

Investigations using a virtual lung model

Max Sharnoff

Trinity 2022

BA Computer Science

Abstract

Detecting changes in human lung morphology and determining its effects on lung function requires significant time commitment per patient, so statistical analysis on many individuals is infeasible. Computational models of the lung are therefore a natural choice for researching the effects of altered lung morphology, with reference to existing lung function tests.

Accurate computational models also allow investigation into properties of the lungs that cannot feasibly be measured; e.g., increased internal stress in one location from damaged airways elsewhere.

This paper builds on recent advancements in modelling airflow in the lungs (e.g., [3]) to create a tool for efficient, accurate computational models of the lungs that supports mid-simulation alterations to lung morphology. We use a fraction of the capabilities of this tool to investigate the effects of whole and partial-lung constriction.

Contents

1	Introduction	3
1.1	Motivation	3
1.2	Contributions to the field	3
2	Background	4
2.1	Physiology of the lungs	4
2.2	Clinical methods	5
2.3	Prior computational models	7
3	Methods	8
3.1	Approximating the lungs	8
3.2	Naive simultaneous equations	9
3.3	Modelling in the abstract	10
3.4	Modified equations for floating-point accuracy	11
3.5	Sparse matrices	12
3.6	Procedural lung generation & configuration	14
3.7	Interpolation functions	15
4	Results	17
4.1	Observed numerical stability	17
4.2	Flow characteristics under stable constriction	18
4.3	Recovery	20
4.3.1	Generalizing recovery	22
4.4	Asymmetric constriction	23
5	Conclusions	24
5.1	Summary of key results	24
5.2	Limitations and further work	25
	Appendices	28
A	Extended equations	28

1 Introduction

1.1 Motivation

Respiratory diseases account for more than 10% of *all* disability-adjusted life-years lost due to any medical condition, second only to cardiovascular diseases (see: [2]). Because of this, any betterment of our understanding of the lungs and how they change from damage can provide immediate benefits towards understanding one of the most significant categories of disease.

In spite of this, there are relatively few existing methods for experimentation. Clinical observations on live patients are necessarily limited, and common techniques – spirometry, inert-gas washout, and MRI imaging – all have severe limitations that render them infeasible or impossible to use for obtaining detailed data on the lungs at scale. And on top of that, the difficulty of drawing inference from these methods is enhanced by the fact that they are purely observational; in this paper, we are concerned with the effects of certain changes in lung morphology (such as: tightening of the airways, stiffness in the expansion and contraction, etc) – effects common to some of the most prevalent lung diseases, like asthma, cystic fibrosis, and chronic obstructive pulmonary disease.

Of course, it would be unethical to *induce* these changes in patients. However, sufficiently-accurate computational models present a natural solution. By designing models that can easily be arbitrarily deformed or otherwise altered, we create the opportunity to efficiently investigate how targeted changes in lung morphology affect both lung functioning as a whole and the stresses placed on individual regions.

Historically, computational models have been severely limited by available resources, but recent advancements in modelling the lungs have shown new methods to be both efficient and accurate, opening the door to a wide range of possibilities.

1.2 Contributions to the field

This paper introduces a new tool for generating computational lung models, simulating them, and changing their morphology mid-simulation. To demonstrate the utility of this tool, we investigate the response of the lungs to various morphological changes, providing this data over a smooth range of possible changes – allowing trends to be plainly visible and inference to be easily made.

2 Background

2.1 Physiology of the lungs

At a high level, the physiology of the lungs can be divided into the few most significant structures. This paper is primarily concerned with modelling airflow, so the intricacies of pulmonary blood circulation or gas exchange are left for the reader to discover elsewhere.

The flow of air into the lungs begins with the diaphragm, a muscle below the lungs that contracts to increase the volume of the *thoracic cavity* (where lungs are housed). The inside of the thoracic cavity and both lungs are lined with a thin membrane – creating a cavity around the lungs when these two layers of membranes are separated. This cavity is the *pleural cavity*, and contains a small amount of *pleural fluid*. The pressure of the pleural fluid – *pleural pressure* – directly drives the expansion and contraction of the lungs, and its values are typically reported as relative to atmospheric pressure.

To keep the lungs inflated, pleural pressure is typically slightly less than atmospheric pressure; the lungs can deflate if the pleural pressure is equal or greater to the air pressure inside the lungs. As the diaphragm contracts to increase the volume of the thoracic cavity, the pressure in the pleural cavity decreases, causing a greater negative pressure gradient, driving inspiration. Correspondingly, typical expiration is driven by relaxation of the diaphragm and the associated increase in pleural pressure from a smaller thoracic cavity.

Air flows into the body through the nose and mouth, meeting the trachea at the larynx, in the neck. The trachea splits into the left and right bronchi – connecting to the left and right lungs respectively. The bronchi split into a binary tree of progressively smaller bronchial tubes (the *tracheobronchial tree*), with the *generation* of a bronchial tube referring to the number of branches between it and the larynx. As the bronchial tubes become smaller, they switch from conducting bronchioles (those that only transport air) to respiratory bronchioles, which attach to and eventually terminate in a small number of acini – small clusters of alveoli. The first respiratory bronchioles are referred to as *transitional bronchioles*, and are generally found around generation 14.[4]

Alveoli are the small, spherical air sacs that act as the sites of gas exchange with the blood. A core technique used in this paper is the approximation of one or many acini as spherical air sacs themselves, further described in subsection 3.1. Typical dimensions for all of the structures above are given in Table 1.

As individual alveoli fill with air, they expand in size. Alveoli are elastic, meaning expanding in volume requires a greater pressure gradient between the air inside and the material outside. One way of referring to this elasticity is by the *compliance* of an alveolus – i.e. how “willing” it is to expand as the pressure gradient increases. There is also a parallel notion of “total lung compliance”, which describes the sum of the compliance of all alveoli in the lung, giving a measure of how the entire lung

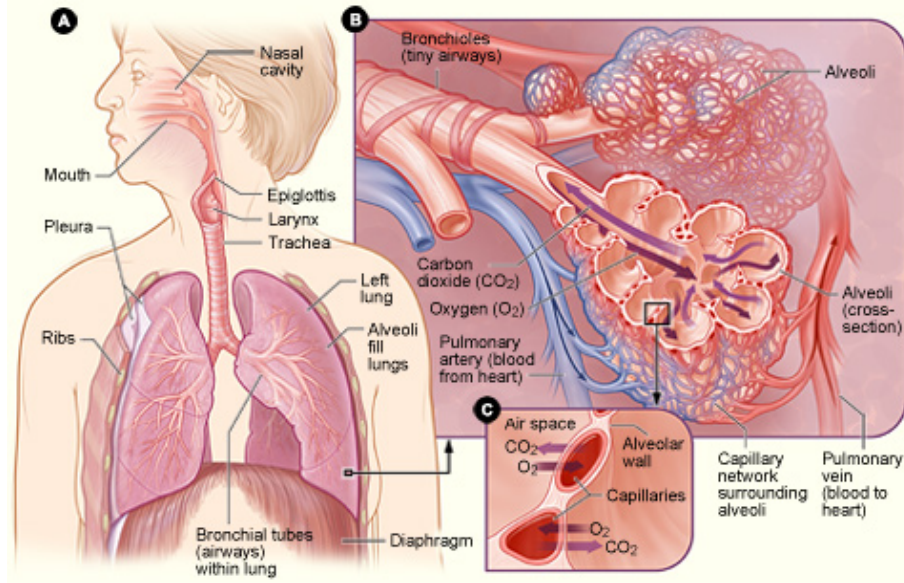


Figure 1: Diagram of the human respiratory system, at three levels of detail: high-level view of the whole system (A), zoomed into a pair of acini (B), and focusing on the site of gas exchange (C). Image sourced from Wikimedia Commons (https://commons.wikimedia.org/wiki/File:Human_respiratory_system-NIH.PNG)

could expand and contract in response to changing pleural pressures.¹

Beyond the structure of the lungs, there are also a number of measures of volume. *Tidal volume* (TV) refers to the volume of air moved in or out of the lungs during a typical breath, and *functional residual capacity* (FRC) refers to the total volume of air remaining in the lungs after a normal expiration.² Typical values for TV and FRC are also given in Table 1.

2.2 Clinical methods

There are a number of relevant clinical methods for measuring lung function, many of which will be discussed in this section. Despite the clinical utility however, there are certain limitations to these methods that make them less well-suited to research, namely: difficulty with establishing causation and cost per datapoint (either monetary, temporal, or both).

Reservations aside, current clinical tools for measuring lung function can essentially be grouped into three categories: exhalation measurement: spirometry and inert-gas washout; oscillometry: FOT and IOS; or imaging techniques: CT, PET, and MRI.

¹Technically speaking, the total lung compliance is related to what the volume of the lung would be if it were filled at atmospheric pressure, given a certain pleural pressure. In practice, there are other factors that prevent the system from equalizing in this way (e.g., airway resistance), and pleural pressure is not typically constant during normal breathing.

²**N.B.:** TV and FRC both describe typical breaths; there are analogous terms for maximum capabilities (*vital capacity* (VC) and *residual volume* (RV)). Also notable is *total lung capacity* (TLC; equal to VC + RV). These are included here for context, but they are not necessary for understanding the experiments in this paper.

Table 1: Average sizes and quantities of lung structures and volumes

Metric	Mean value (adult female)	Mean value (adult male)
Trachea length	9.8 cm [8]	10.5 cm [8]
Trachea radius ^a	0.91 cm ^b [7]	0.98 cm ^b [7]
Trans. bronchiole length	1.33 mm [4]	
Trans. bronchiole radius	0.25 mm [4]	
Acinus volume	approx. 187 mm ³ ^c [4]	
Number of acini	30,000 [20]	
Alveolus volume	0.0042 mm ³ [10]	
Number of alveoli	approx. 480,000,000 ^d [10]	
TV	400 mL [5]	500 mL [5]
FRC	2.64 L ^e	3.50 L ^e

^a Measurements are highly dependent on lung volume at time of measurement.[7] These values are at 50% of VC, typically closer to FRC than TLC. Other studies provide higher-accuracy measurements, but at TLC.[14]

^b Calculated from airway cross-sectional area data, assuming circular cross-sections, *then* averaged.

^c Data on this is limited; the actual mean may be quite different.

^d Variability in number of alveoli is very high (stdev $\approx 180 \times 10^6$), is unrelated to lung size, and density of alveoli is the same between boys and girls, so it is unclear whether there are sex differences. [10, 17]

^e Adapted from [9], via unweighted average across all age groups.

Spirometry measures the volume and flow from a patient’s maximal exhalation (after maximal inhalation), producing volume-flow and volume-time curves. It is simple to perform, but the reliance on maximal exhalation gives it a particularly low sensitivity. *Inert-gas washout* instead floods the lungs with an inert gas (e.g. SF₆ or ³He) before continuously measuring the concentration of the gas exhaled through normal breathing. Measurements are either made over many breaths (*multiple-breath washout* (MBW)) or just one (*single-breath washout* (SBW)). Both MBW and SBW have a number of indices typically produced from the data, which correlate with many lung diseases.

Both *forced oscillation technique* (FOT) and *impulse oscillometry* (IOS) apply oscillations at the mouth and measure the resulting airflow and pressure. FOT uses controlled pulses whereas IOS uses pseudo-random noise. From this, estimates of resistance and inertance of the lungs are made, which have correlations to diseases such as asthma and COPD.

Finally, we have the imaging techniques: *Magnetic resonance imaging* (MRI), *computed tomography* (CT), and *positron emission tomography* (PET). Beyond immediately visible ailments (e.g. foreign objects or fluid buildup), these methods can also be used to estimate the ventilation of air in each voxel of the image – providing metrics that can quantify overall lung function (and highlight specific regions where function is degraded). However, these methods are typically expensive (MRI)

or dangerous in large amounts (CT and PET) and the timeline of resolution improvements means that high-resolution imaging has not been available for as long as other methods. The costs associated with these methods and the relative recency of high-resolution versions has meant that there is also a relative gap in the literature linking imaging results to respiratory disease classification.

This final point is one of the key reasons why computational models are so useful; high costs or low availability hinder new research, and computer simulation can provide a simpler, cheaper method for testing ideas. It is difficult to obtain large amounts of data for analysis when the underlying methods are expensive or time-consuming, relative to the amount of data produced.³

Also of note is that all of the above techniques are strictly observation with respect to the condition of the lungs. Analyzing the effects of various morphological changes within the lungs is difficult without the ability to directly effect those changes, but forced changes to patient lung morphology are typically both risky and unethical.

For those reasons, it is natural to turn to simulations – in particular, computational models – in order to gain insight into impact on physiology and overall function from isolated changes within the lungs.

2.3 Prior computational models

This section is unfortunately brief – historically, computational models have been limited by the available resources (they still are) and data to base them on. From the beginning, simulating “full” fluid dynamics with the Navier-Stokes equations has been both unnecessary and out of reach; reasonable assumptions can be made about the flow of air within the lungs to simplify modelling (see: subsection 3.1), and models have increased in complexity over time to match advancements in the speed of computers.

Early models represented the lungs with just a few elastic chambers, but advancements in physiological data (particularly from [19]) allowed later studies to generate larger models of the lungs, with the size now singularly limited by computational capabilities. However, general models remained untouched for many years after. A brief survey of the time between shows: a model of individual alveolar ducts from 1974 ([11]), a couple models specific to multi-breath washout from 1990 and 2001 ([18] and [16]), and a model of ³He gas diffusion – among many others not mentioned here.

More recently however, there was a 1-dimensional asymmetric branching model from 2012 ([6]) and a *different* 1-dimensional from 2017 that this paper builds on ([3]), using partial construction of from patient imaging (up to generations 6-10) – both of which model the lungs as a whole, directly.

In summary: computational models of the lungs as a whole are still relatively new; in this paper we investigate some areas of untapped potential for these recent computational models.

³To be clear here: methods like spirometry are relatively cheap and not overly time-consuming, but the amount of data each test generates is small; establishing complex relationships may require large amounts of data, regardless of the type of test used.

3 Methods

Broadly speaking, this section comes in two parts; first defining the more theoretical underpinnings of the model used for simulation throughout the rest of the paper, followed by some detail on the implementation in practice. Much of the theory is adapted from the airflow model used in [3], with minor modifications.

At a high level, we approximate the structure of the lungs *acinar regions* and represent the effects of the diaphragm as a uniform *pleural pressure* outside these acinar regions. The simulation itself uses the implicit Euler method, giving strong numerical stability at the cost of solving a complex system of equations (Equation 4) at each timestep.

At the implementation level, we modify the initial naive equations above to improve floating-point accuracy, and demonstrate the benefits of using sparse matrices – even without a particularly complex solver method.

3.1 Approximating the lungs

As with any computer simulation of physical processes, approximation is required on some level, due to the inherent limitations of classical computers. There are three distinct simplifications made for the purposes of computational feasibility that we will discuss here.

First, however, it is worth establishing some terminology: When referring to the simulated components of a lung, we use the term *branch* instead of bronchiole because the meaning is intended to be slightly different. All models are composed of bifurcation branches (those that split into two child branches) and acinar branches (akin to a terminal bronchiole and the attached acinus).

With terminology out of the way, the first simplification is that we assume our airflow is one-dimensional and incompressible. Modelling air inside the lungs as three dimensional or compressible could be more accurate, but would also require significantly more computational resources. Prior studies have shown that making this simplification retains the accuracy of the model – the small-scale differences that may arise when compared with actual lungs do not appear to affect the large-scale behavior.

We also simulate groups of many acini at once by modelling them as a single, balloon-like air sac. With the average pair of human lungs containing approximately 300 million acini, assigning a unique set of variables for each one would be infeasible on even the most powerful consumer-grade computers. So we approximate arbitrarily large numbers of acini as *acinar regions*, modelling their elastic behavior and interaction with the pleural pressure in the same way as individual acini would be modelled.

And finally, we assume that the influence of gravity on pleural pressure is negligible. Prior studies have shown that a gradient in pleural pressure from gravity exists, and [3] use a gradient for pleural pressure in their model. We chose to omit this for simplicity, due to the relatively small magnitude of these gradients⁴ – though it could be added to the model with little effort. Without this gradient, the position

of each branch in a given model has no effect on the mechanics of its simulation.

3.2 Naive simultaneous equations

This section provides a summary and brief description of the four simultaneous equations that govern the state of our simulation, before the modifications made in subsection 3.4. Together, the system of equations must be solved at each timestep to determine the current state. The first equation is the following:

$$P_{\text{parent}(i)}^{t_n} - P_i^{t_n} = R^{t_n}(i)Q_i^{t_n} \quad (1)$$

This specifies that the pressure differential between the distal end of branch i and its parent must equal the pressure from the resistance from the flow through this branch i . For the “root” branch, $P_{\text{parent}(i)}$ gives the pressure at the trachea – typically atmospheric pressure. Additionally, all variable terms are parameterised by the current time t_n .

The resistance term $R^{t_n}(i)$ for a branch i is defined as following function, as given by [13]:

$$R^{t_n}(i) = \frac{2\mu L_i C}{\pi r_i^4} \left(\frac{4\rho |Q_i^t|}{\mu \pi L_i} \right)^{\frac{1}{2}}$$

The parenthesized term corresponds to the Reynold’s number of the flow, scaled by the ratio of the diameter of the branch to its length L_i . r_i is the radius of the branch, μ is the viscosity of the air, and $C = 1.85$ is a correction constant originally derived by the same authors in [12].

The second equation comes as a restriction from incompressibility: the flow through a bifurcation branch must equal the sum of the flow through its children:

$$Q_i^{t_n} = \sum Q_{\text{child}}^{t_n} \quad (2)$$

where each *child* refers to any branch c with $\text{parent}(c) = i$.

The third equation maintains that the volume of an acinar region changes with the flow into or out of it for the given timestep:

$$V_i^{t_n} = V_i^{t_{n-1}} + dt Q_i^{t_n} \quad (3)$$

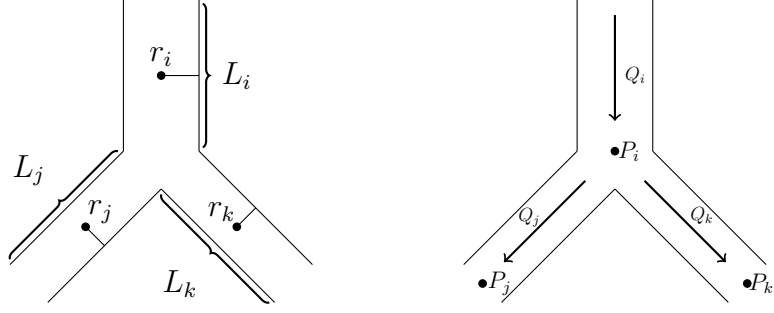
where dt is the timestep size, t_n refers to the current timestep, and V_i is the volume of the acinar region of branch i .

The final equation defines the elastic force of each acinar region, relating the pressure it exerts on its branch to the volume of the region itself and the pressure outside it:

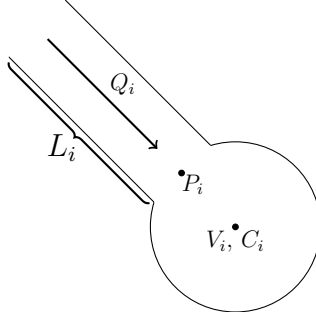
$$P_i^{t_n} = \frac{1}{C_i} V_i^{t_n} + P_{\text{pl}}(t_n) \quad (4)$$

where $P_{\text{pl}}(t_n)$ gives the pleural pressure at the current time and C_i is the compliance of the acinar region of branch i . The pleural pressure changes over time to mimic

⁴[3] draws upon prior studies to use a gravitational gradient strength of 1.5%/cm.



(a) Bifurcation from parent branch i to children j and k , both dimensions (left) and state (right).



(b) Acinar region and attached branch

Figure 2: 2-dimensional cross-section of a modelled bifurcation (a) and acinar region (b), labelled with the values composing the equations in subsection 3.2.

human breathing patterns, and is independent of the state of the lungs – hence why it is parameterised by t . The pleural pressure for a given simulation follows a sinusoidal function given by its initial, minimum, and maximum values and its period T . This function is defined in Appendix A, and typical values are given in section 4.

3.3 Modelling in the abstract

We use an *implicit* Euler method to model the system as it progresses: at each timestep, our simulation updates its state to the value of an approximate solution to the system of equations above. Equation 4 provides the necessary bounds to make the method implicit, giving us higher accuracy at the cost of implementation complexity.

To solve for an approximate solution at each timestep, we use Newton’s method with $f_{\mathbf{S}}(\mathbf{x})$ as defined below, iterating until $\|f_{\mathbf{S}}(\mathbf{x})\|^2 \leq tol$ and $\|dx\|^2 \leq tol$, with a tolerance of 10^{-6} . The two “inputs” – \mathbf{S} and \mathbf{x} – partition the state of the model into the variables that are controlled externally (e.g.: pleural pressure, compliance) and those that are calculated from the system state (e.g.: acinar volume, airflow). The definitions of \mathbf{x} and $f_{\mathbf{S}}$ are given by:

$$x = (P_i..., Q_i..., V_i...)$$

$$f_{\mathbf{S}}(\mathbf{x}) = \begin{bmatrix} P_{\text{parent}(i)} - P_i - R(i)Q_i \\ \vdots \\ Q_i - \sum Q_{\text{child}} \\ \vdots \\ V_i^t - V_i^{t-1} - dtQ_i^t \\ \vdots \\ P_i - P_{pl}(t) - \frac{1}{C_i}V_i \\ \vdots \end{bmatrix}$$

Note that the values in \mathbf{x} and equations in f are repeated only as many times as fits; e.g., there are fewer acinar regions than total branches, so there are fewer components in \mathbf{x} from each V_i than from each Q_i .

As \mathbf{S} only exists in the abstract sense, we won't bother to define its structure; all that's necessary to know is that it contains every variable referred to in f that is not already given explicitly by \mathbf{x} .

It's worth noting that in practice, the above definitions are only *nearly* correct; a few adjustments were made to the inputs and equations to mitigate limitations from floating-point accuracy. These are discussed in the next section.

3.4 Modified equations for floating-point accuracy

During initial experimentation, it became apparent that – under certain conditions – the pressure differential between ends of the bronchial tubes became too small for floating-point calculations to represent the changes in pressure during updates from Newton's method. This was because the absolute magnitude of the pressure (around 1e6 Pascals) was significantly different from the differences in pressure (much less than 1 Pascal).⁵ We mitigated this by changing the formulation of the equations used in the simulation, improving their accuracy without changing their semantic meaning.

The “new” equations gain accuracy by centering values closer to a magnitude of 1, so that the required number of significant digits is greatly reduced.⁶ These equations use two new values, \hat{P} and \hat{V} , that are relative to atmospheric pressure. They are defined by:

⁵**N.B.:** The change in pressure from *timestep-to-timestep* was still large enough to represent, but the changes to dx during the Newton iteration were. While it initially resolved by the methods in this section, this problem would have also been far lesser with 64-bit floating-point values (which we did eventually switch to).

Please also note: The approximate pressures described here might be, but are not necessarily, reflective of pressures in the final simulation; there were multiple issues fixed after this observation that may have impacted these values. Even still, the modification was kept, as it provided a non-zero benefit.

This problem was detected while simulating unrestricted models, where the relative ease of flow means that the pressure throughout the lungs remains much more balanced.

⁶Floating-point numbers have a fixed number of significant digits; arithmetic operations with large differences in magnitude tend to lose significant information in the process.

$$\hat{P} = P - P_{\text{atm}} \quad (5)$$

where P_{atm} is atmospheric pressure; and:

$$\hat{V} = V - V|_{P=P_{\text{atm}}} \quad (6)$$

$$= C(\hat{P} - P_{\text{pl}}) \quad (7)$$

Note that the definition of \hat{V} would be the result of simply substituting \hat{P} for P in Equation 4. Applying these substitutions gives the following equations, equivalent to their counterparts above:

$$\hat{P}_{\text{parent}} - \hat{P}_i = R(i)Q_i \quad (8)$$

$$Q_i = \sum Q_{\text{child}} \quad (9)$$

$$\hat{V}_i^t = \hat{V}_i^{t-1} + dtQ_i^t \quad (10)$$

$$\hat{P}_i = \frac{1}{C_i}\hat{V}_i + P_{\text{pl}}(t) \quad (11)$$

Representing the pressure and volume by their *offset* from values at atmospheric pressure causes them to cluster much closer to zero – the magnitude of the mean is significantly decreased, relative to the variance of the values. This of course greatly improves the accuracy of each Euler step.

The same substitutions also apply to our representations of the state of the model and the optimization function used for Newton’s method, as shown in subsection 3.3.

3.5 Sparse matrices

A key observation that aiding in simulation speed is that the Jacobian of our optimization function f has only $\mathcal{O}(n)$ entries – which allows for dramatic storage space and runtime savings. This optimization is crucial for practically running simulations up to a high depth on a single computer.

We used sparse matrices, solving the equations with a sparse Gaussian elimination. Other methods (such as GMRES) were initially considered but not used, due in equal parts to lack of library support and the sufficiency of the simpler Gaussian elimination.⁷ The increase in execution speed from dense to sparse matrices is quite significant, as demonstrated in Figure 3. The observed time for a simulation tick – which is roughly proportional to the time spent solving the system of equations – is still not linear in the number of nodes, however: fitting the sparse matrix timings to a power series model gives an exponent of 1.97 and R^2 of 0.989. Fitting a power series to the dense matrix timings gives an exponent of 3.35 and R^2 of 0.997; clearly significantly worse.

⁷There are, of course, *many* sparse matrix libraries in existence. The project was written in Rust, which – at time of writing – did not have more advanced sparse matrix solvers.

Time to calculate simulation tick, dense vs sparse matrices

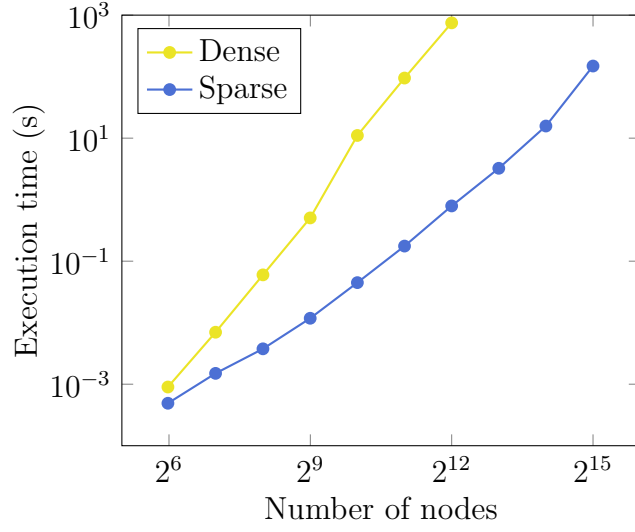
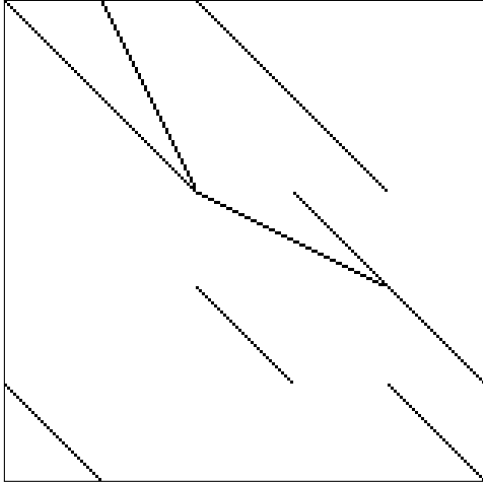
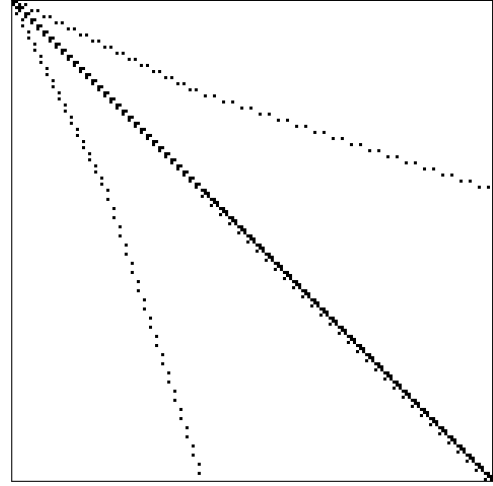


Figure 3: Time to compute a single simulation tick, with dense versus sparse matrices. Models were simulated for 10 ticks in total, with the results above taken as the average of the final 5, to reduce the impact of operating system caching on performance.



(a) The sparsity pattern of Jacobians as implemented



(b) A possible “cleaner” sparsity pattern, arranging variables for each node at consecutive indexes.

Figure 4: Comparison of the implemented sparsity pattern with one possible alternative (of many). 4b is not *necessarily* more efficient; it demonstrates that other options were available, as an area of possible improvement.

Although the improvement from $\mathcal{O}(x^{3.35})$ to $\mathcal{O}(x^{1.97})$ is significant, it is possible that other orderings of values within the Jacobian may be better-optimized for sparse Gaussian elimination. Figure 4 provides a visual comparison between the sparsity pattern that was used in the software developed for this paper and a hypothetical alternative. The current layout used places all variables and equations of a certain type at consecutive indexes, i.e. $(P \dots, Q \dots, V \dots)$ instead of e.g. $(P_0, Q_0, V_0, P_1, Q_1, V_1, \dots)$, with variables and equations for parent nodes occurring at *later* indexes.

As context for Figure 4 however, it is important to note that it is not possible for the system of equations to be simply organized into an upper- or lower-triangular matrix; each equation is composed of at least two variables. With this option unavailable, we did not assess alternate orderings of values within the Jacobian.

3.6 Procedural lung generation & configuration

As part of the simulation software developed for this paper, there are a number of configurable parameters – primarily encapsulating the structure of the lungs and how they change over the course of the simulation. Listing them exhaustively, the parameters are:

- Lung structure (the tree formed by the relationship between branches)
- Approximate typical lung FRC
- Branch length, as relative to the parent
- Branch radius (healthy & degraded), relative to the parent
- Acinar region *relative compliance* (healthy & degraded)
- Branch angles (only affects the lungs’ appearance)
- Keyframe-based scheduling to shift the lung state between healthy & degraded
 - Multiple interpolation functions to transition between keyframes
- Pleural pressure wave characteristics (initial value, mean, amplitude, and period), as well as the “normal” maximum value (see below).

The specification of “healthy” and “degraded” allows us to define and transition between two states of the lungs, simulating the onset and treatment of the affects from many respiratory illnesses. The speed of onset or recovery is controlled by the positioning of the keyframes, which are binary “healthy” or “degraded” states. These states do not directly affect the simulation state, i.e. the flow, pressure, and acinar volume within each branch. This does mean that, for example, the pressure in constricting airways does not increase directly as a result of that constriction, but we have considered the volume inside the branches themselves largely negligible. The most important factor is that the volume within each acinar region is conserved, which *is* guaranteed, even across changing compliance.

It is also worth clarifying the meaning of *relative compliance* in the list above. In order to ensure that the total volume of the lungs remains consistent with human anatomy, the compliance of each acinar region is linearly scaled so that the total volume from all acinar regions filled at atmospheric pressure would give the configured FRC of the lungs at the “normal” maximum pleural pressure (a separately-configurable value). For typical values (e.g. those described in section 4), the total lung compliance is approximately $2.0 \times 10^{-6} \text{m}^3/\text{Pa}$ (approximately 0.2 L/cmH₂O).

The details of the configuration format itself are outside the scope of this paper, but the configurable values are described here to provide context for the parameters that were varied in the experiments we report. A number of these parameters actually were never experimented with, due to scope of the project.

3.7 Interpolation functions

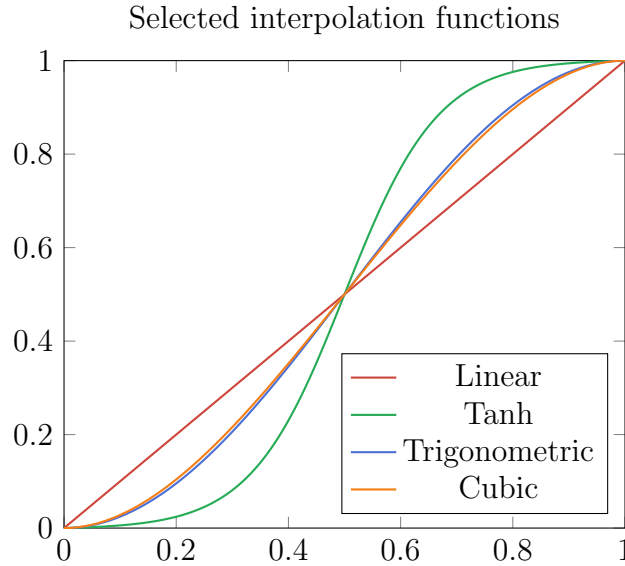


Figure 5: Comparison of the four selected interpolation functions

A number of later experiments transition between differing levels of airway constriction with the use of *keyframes* – a set of (time, constriction) pairs defining a handful of states that must be reached. To define the intermediate values between these states, we have four different interpolation functions:

- *Linear*: $f(x) = x$
- *Tanh*: $f(x) = \frac{1}{2} \frac{\tanh(6x-3)}{\tanh(3)} + \frac{1}{2}$
- *Trigonometric*: $f(x) = \frac{1}{2}(1 - \cos(\pi x))$
- *Cubic*: $f(x) = 3x^2 - 2x^3$

A visual comparison of these functions is provided in Figure 5.

These functions were selected as options for their relative simplicity and variety of curvatures. While we could change these parameters instantaneously, there were a couple reasons to have smooth transitions – primarily to avoid instantaneous jumps in flow or volume, but also because processes that would affect the lungs in this way are very unlikely to be instantaneous themselves. If we *do* need to model a near-instant change, keyframes already allow us to make the transition period arbitrarily short.

Some amount of curvature is also desirable – although perhaps not necessary: without a continuous derivative, there are often unusually sharp changes in the rate of flow. This is perhaps intuitive, but still worthwhile to point out.

Finally, it is worth noting that the correction factor of $\tanh(3)$ in the denominator of the *Tanh* interpolation function is nearly equal to 1, but still necessary. The value of $\tanh(3)$ is only 0.995, but experiments without that correction factor showed clearly visible jumps in the rate of flow from that small change. While these changes were most likely harmless, we still elected to remove them.

4 Results

Before properly describing the results, it is worth providing some context for the typical parameters used for running the various simulations. Unless otherwise indicated, we use the following values: approximate FRC of 3 L, trachea length of 10 cm, trachea radius of 0.95 cm, pleural pressure range from -875 to -750 Pa with a period of 4 seconds, bronchiole length decrease of 27% per generation, bronchiole radius decrease by 23% per generation, and a depth of 10 generations (i.e. 512 acinar regions). The depth was limited by the computational resources required to simulate hundreds of different models.

Values for the trachea are taken as a middle-ground from Table 1 and bronchiole size decrease is derived so that the same fractional decrease per generation results in the appropriate sizes at transitional bronchioles (also from Table 1). The pleural pressure is adapted from [1], using an idealized model of elasticity for an approximate tidal volume of 0.5 litres.

We typically use a timestep of 0.01s for the simulation, with smaller timesteps sometimes used to get higher-fidelity output (e.g., for Figure 8).

4.1 Observed numerical stability

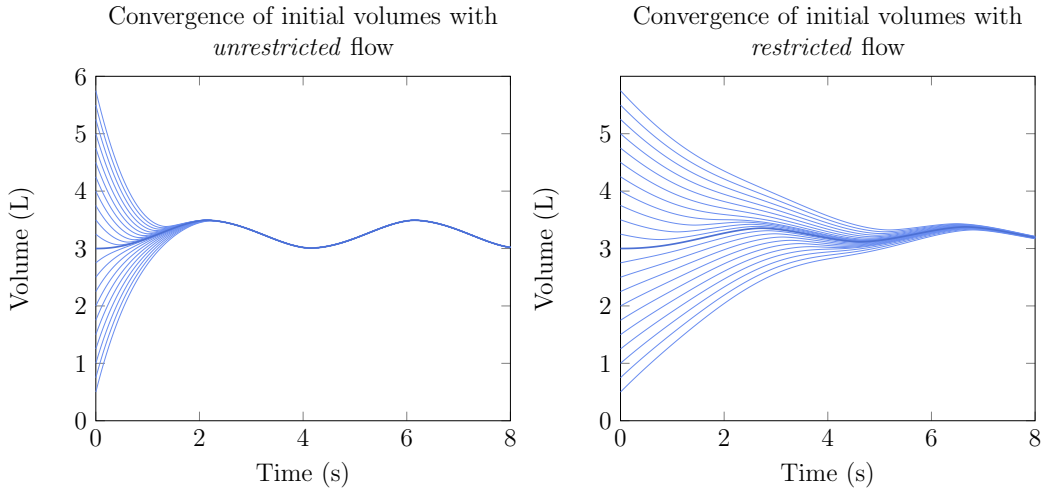


Figure 6: Simulated volume at the start of a breathing cycle, with varied initial volumes. Both experiments with a symmetric model with a depth of 10 generations. Graphs display the distinction between unrestricted (left) vs 40% constricted (right). **Note:** displayed timespan differs between the left and right graphs.

To be confident in the results of other experiments, it is first crucial to determine that the simulation remains stable after running for extended periods of time. To do this, we simulated a simpler model (fully symmetric, no constriction, depth of 10) for 1000 seconds – which required 100,000 simulation ticks.

It is at this point that we’d ideally reference some figure to show that the system is stable in this configuration, but the series of volumes at each timestamp – starting at 4, 100, and 1000 seconds – were all the same, up to nine significant figures. By

the end of the first breath cycle, the volume had corrected from the starting volume of 3 to 3.019 litres. Total volume of air in the lungs over the course of each “breath” did not change over the course of an atypically lengthy experiment, indicating a high degree of numerical stability (as expected, due to our use of an implicit Euler method).

We also considered that the initial volume used in experimentation is not guaranteed to be accurate to the “typical” volume at that point in the breathing cycle – a fact that becomes visible with higher degrees of airway constriction (discussed in subsection 4.2). Therefore, we also experimented with significantly changed initial volumes, as shown above in Figure 6. The system quickly recovers from perturbations when airflow is unrestricted, but is slower to return to the typical volume when resistance prevents the correction from being made more quickly.

4.2 Flow characteristics under stable constriction

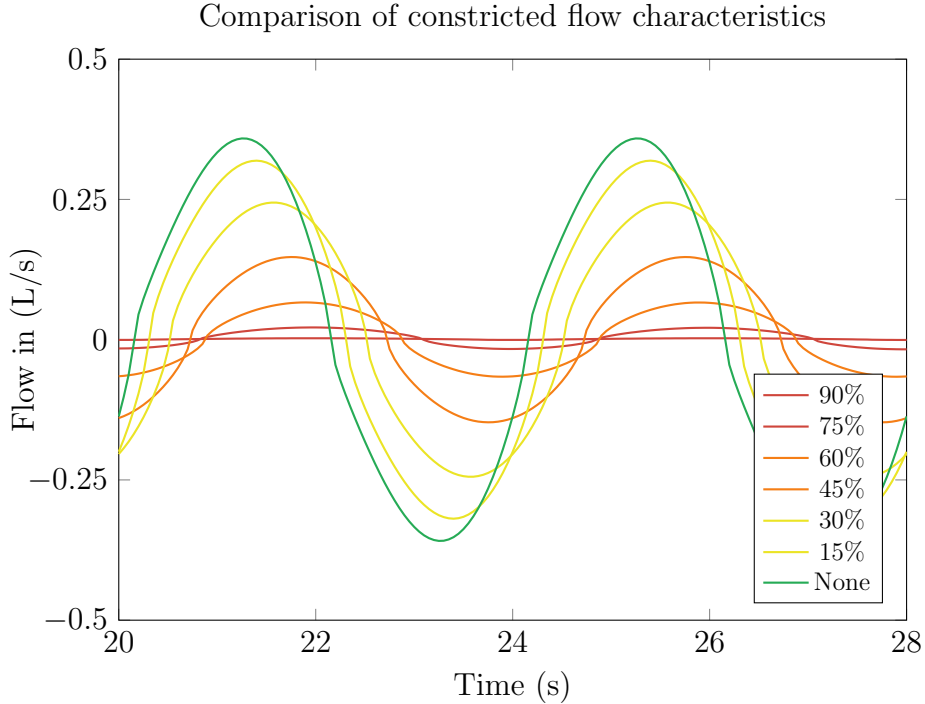


Figure 7: Stable flow during two breathing cycles with varied levels of whole-lung airway constriction. Measurements were only recorded after 20 seconds to ensure the effects of any starting conditions had been minimized, shown necessary at severe constriction by Figure 6.

The first set of experiments investigated the behavior of sustained, normal breathing under minimal to severe constriction. Here, we used whole-lung constriction – limiting the radius of all airways by a given fraction. Figure 7 displays the recorded airflow at the larynx for normal breathing under a few different levels of constriction. The function determining pleural pressure was kept constant.

As constriction increases, there are three visible effects: the maximum flow decreases, the time of the peak in flow shifts later, and the shape of the flow curve also changes – becoming flatter at its peaks and troughs and steeper around the transitions between positive and negative flow.

Figure 8 quantifies these effects, with additional data provided for dilation of the airways. Our analysis here includes the range of airway widths covered by dilation because it provides information that may correspond to humans with naturally wider airways.

Maximum flow slowly decreases from 50% dilation to none, after which it curves more steeply towards zero. However, before the *amount* of flow changes significantly, the effects of constriction are readily visible in other characteristics of the curve – particularly the maximum acceleration: it increases from 50% dilation to around 10% constriction, at which point its magnitude starts to become limited by the height of the flow curve.

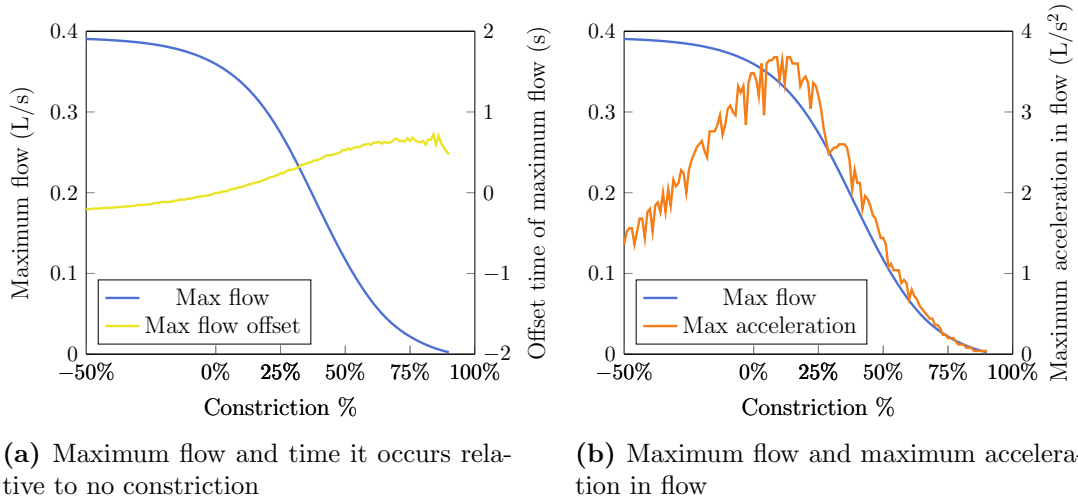


Figure 8: Changes in airflow characteristics as constriction increases from dilation by 50% to 90% constriction. Peak airflow is displayed as a baseline for both the time maximum flow occurs (left) and the maximum acceleration in flow between simulation ticks (right).

Some unevenness is present in the graph of maximum acceleration. Initially, this was thought to be due to the particular way that it is being measured, namely: finding the greatest increase in flow from one simulation tick to the next. Slight differences in the timing could have meant that the maximal acceleration had some local variability despite the global trend.

To test this, we ran the simulation with a timestep of 1/400s instead of the usual 1/100s, the results of which are in Figure 8. The peak is much greater (up from approx. 2 L/s² to approx. 3.5), indicating that there was a degree of the most extreme points not being captured. This may still be the case, even at 1/400s – as improbable as it seems.

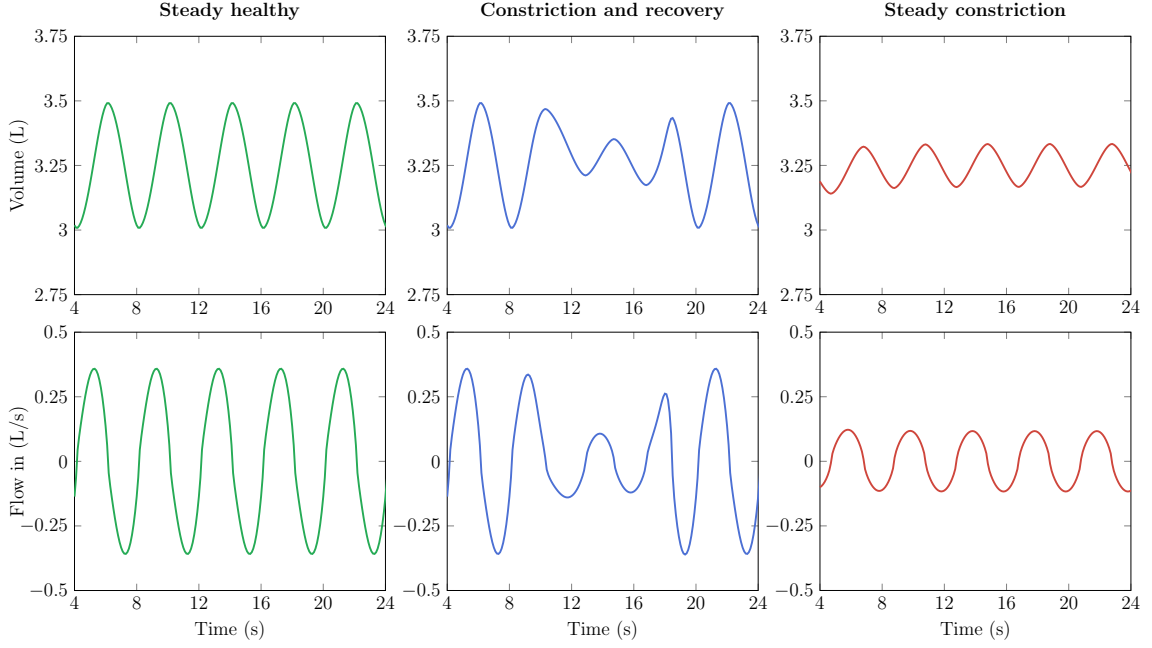


Figure 9: Side-by-side comparison between unconstricted flow (left), gradual constriction and recovery (middle), and constricted flow (right). The target constriction level was 50%, with `tanh` used for interpolation. For the recovery, transitions between constriction levels were 4 seconds each, onset was at 8 seconds, and recovery started at 16 seconds.

4.3 Recovery

Using the scheduled constriction feature of the software made for this project, we ran a number of trials that started with a “healthy” lung, then slowly constricted the airways to a target constriction (smoothing with interpolation functions from subsection 3.7), stayed constricted for a full breath, and then gradually reduced constriction back to the healthy state.

An example of this is given in Figure 9, with baseline comparisons for the flow and volume of the lung under no constriction or the target of constriction by 50%. All three models were run for 4 seconds at the start to even out any disturbances from the initial state. At 8 seconds, the recovery trial starts to constrict, but it only starts to become noticeable at around 11 seconds (discounting the raised trough at 9 seconds) – before finally reaching the target constriction at 12 seconds. From there, the flow appears nearly identical to the constricted baseline, with a slightly higher than baseline flow briefly at the 12 second mark. In a similar fashion, recovery starts after a full breath cycle, at 16 seconds. The effects of reducing constriction are almost immediately visible, with an unusually sharp increase in flow at 18 seconds. At 20 seconds, the constriction has been fully removed and flow appears normal.

There is a lot of information in the above paragraph – to summarize briefly: the most visible effect in this trial of changing constriction levels is that volume and flow tends to quickly match the characteristics that we would expect from the constriction level it reaches. Some atypical behavior *is* observed around these transitions, but it is brief (e.g., the flow at 18s).

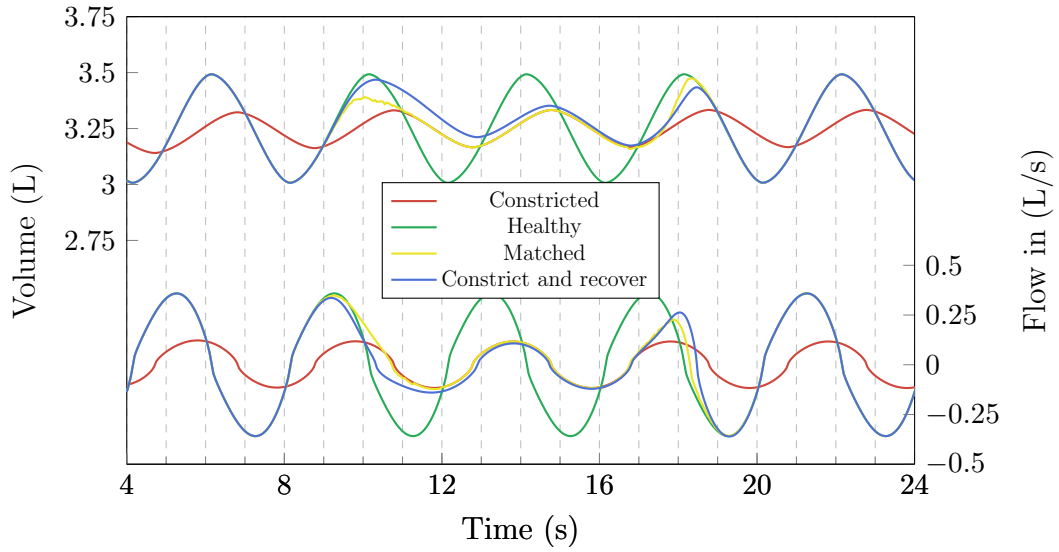


Figure 10: The same recovery trials from Figure 9, compared with the values of volume and flow corresponding to a stable breath pattern at the current constriction level, at each point in time (“Matched”). Much of the jaggedness is due to the imprecision in linearly interpolating between the two closest constriction trials (to the nearest integer percentage).

To demonstrate the causes behind this atypicality, Figure 10 overlays the recovery and baseline trials with a sort of “matched baseline” – composite curves made by taking from the baseline curve matching the constriction level each datapoint. For example: at 10 seconds, the model is constricted by 25%, so the “matched baseline” at 10 seconds uses the flow and volume from a steady run at 25% constriction at 10 seconds.

Looking at Figure 10, it’s tempting to think that the recovery trial directly follows the matched baseline. However, while changing the constriction level (i.e. airway radii), the only variable that remains different between trials is the volume; everything else is derived from the airway morphology and pleural pressure, the latter of which we have kept consistent. The simulation has no “knowledge” of the appropriate volume to correct to.

Instead, the matching *must* be a direct result of the way that the flow due to the current volume and pleural pressure is limited (or allowed) by the airway widths. With greater constriction, the flow becomes more limited by resistance from smaller airways, which is why we see a reduced tidal volume, even though the compliance and pleural pressure haven’t changed.

When recovery is introduced, this effect tends to *imitate* the matched baseline, but only where the volume is already similar – and changes in volume are limited by airway resistance. This is most visible in the way that the recovery trial stays distinctly separate from the constricted baseline for most of the period in which it is at that constriction level: the initial raised volume takes time to correct for.

The effects at 18-19 seconds are similar in nature: the recovery trial initially diverges from the matched baseline because its volume at, e.g., 17.5 seconds is less than would be expected for the level of constriction at 18 seconds. Because of this difference, the recovery trial maintains inward flow for longer as the pleural pressure

starts to increase. Eventually at 18.5s, the slowed upward trend in volume meets the matched baseline and snaps to the same flow – because the volume and pleural pressure are the same.

4.3.1 Generalizing recovery

All of the above serves to illustrate some of the ways in which flow can be disrupted by actively changing the level of whole-lung constriction. There are a couple of general findings to note.

Firstly: airway size matters, both “healthy” and constricted. In our early experimentation, we found that unusually wide airways – precisely because they have so little resistance – can easily result in large spikes in airflow as out-of-phase constricted volume is adjusted with loosening constriction and large negative pleural pressure.

Secondly, the precise nature of the abnormal flow that we see when recovering from constricted airways varies greatly depending on the timing (relative to each breath) and speed of the recovery. This can similarly be selected to produce similar effects as above, as demonstrated in Figure 11. Abnormally high flows can be created from normal pressures simply by forcing the volume to remain mostly constant as the pleural pressure changes beneath it. This is essentially akin to breathing in, closing the epiglottis, fully relaxing the diaphragm, and then opening the epiglottis – releasing the air quicker than would normally happen as the diaphragm slowly relaxes.⁸

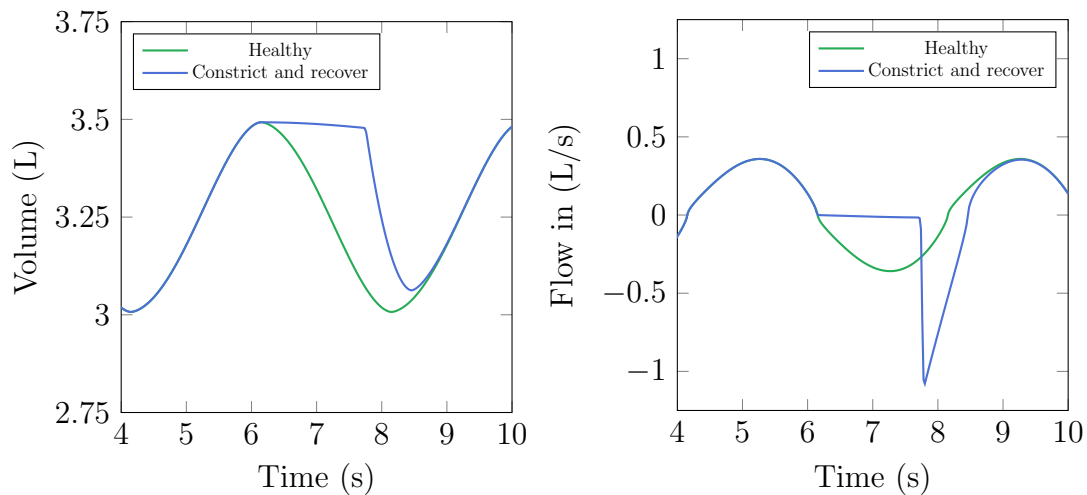


Figure 11: Extreme example of timed severe constriction (by 80%) causing large spikes in flow. Constriction begins at 6.1s, takes full effect within 0.1s, and starts returning to normal at 7.7s, also taking 0.1s.

Of course, the type of breathing shown in Figure 11 is highly unlikely to happen in practice – primarily because real humans will tend to react to their internal lung

⁸In practice, this demonstration tends not to be very extreme (due to the diaphragm moving slowly even when relaxed). A more sudden example is the reverse: contracting the diaphragm without breathing in, then allowing air to enter the lungs.

state by indirectly changing the pleural pressure in a way that our model cannot. This is discussed in more detail in subsection 5.2.

4.4 Asymmetric constriction

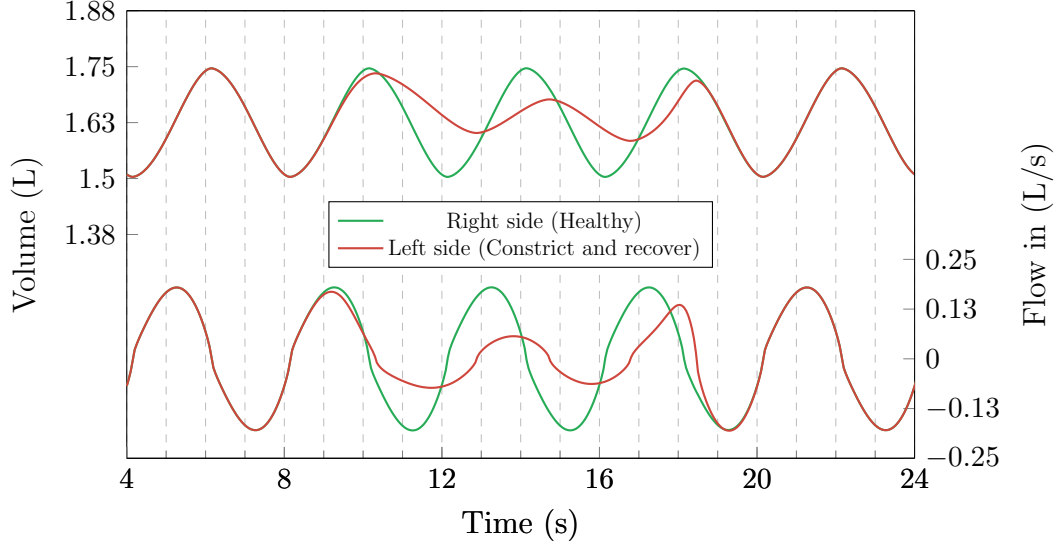


Figure 12: Asymmetric constriction and recovery, with onset of left lung constriction at 8s, reaching the final 50% constriction by 12s via \tanh interpolation, and recovering from 16-20s.

The final experiment performed was around the use of asymmetric constriction. We ran the same trial as from Figure 10, but limited the constriction to just the left side of the lung. The separate volume and flow between the two equal halves are paired in Figure 12.

Interestingly, the right lung appears completely unaffected by the reduction in flow from the left lung. While the left lung appears to have identical flow characteristics as the trial from Figure 10, the right lung equally appears to have the characteristics of a healthy lung. This seems to imply that the resistance terms primarily limiting faster flow in the right lung are *not* coming from the trachea; otherwise the reduced flow from the left lung would have eased that resistance and allowed faster flow from the right lung.

There is, however, an imperceptibly small difference between the flow from the right lung in this trial, and one where the left lung remained healthy the entire time: At 50% constriction in the left lung, the maximum flow through the right lung is 0.3 mL/s greater than with no constriction – and at one point in time, the difference between the two flows is 8.1 mL/s.

Clearly these are still small, but it is worth quantifying these differences and observing how they change with constriction; so Figure 13 displays both of these metrics. With a quick look at the two charts, it is clear that even with the most severe constriction on the left lung, the flow through the right lung barely changes, supporting the initial observations from Figure 12.

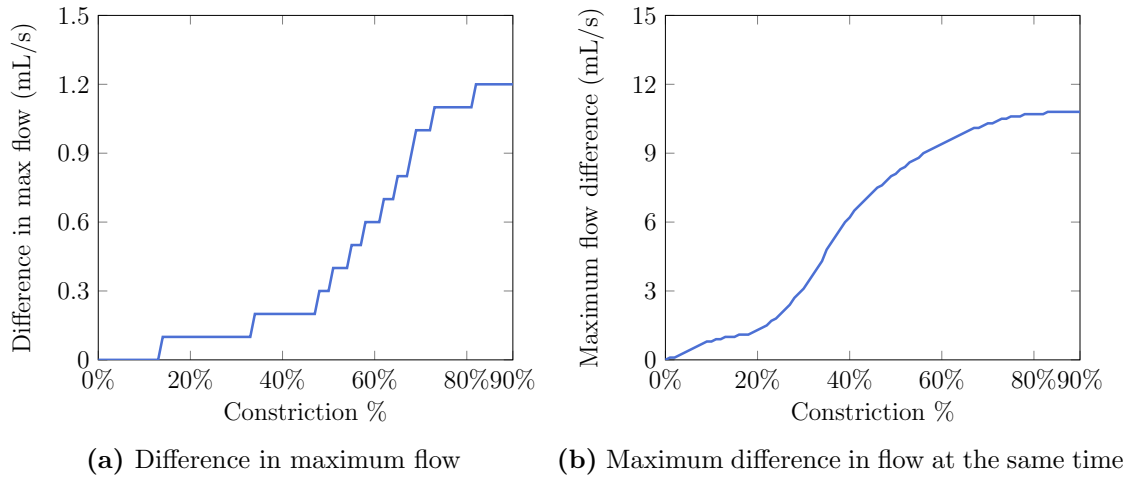


Figure 13: As constriction in the left lung increases, comparisons of the flow in the right lung with a right lung from a healthy left lung. **N.B.:** Units are measured in millilitres; the differences are very small.

5 Conclusions

5.1 Summary of key results

In this paper, we have used recent, established mathematical models to investigate the characteristics of airflow in the lungs under a variety of conditions. In particular, we’ve demonstrated a clear association between maximum acceleration in flow and airway constrict, in a way that is not as visible in just the maximum speed of flow reached.

From there, we introduce the “constrict and recover” pattern, where the airways in an initially-healthy lung are gradually constricted to a desired level and after a delay, they gradually return back to the healthy state. The flow characteristics as the constriction level changes appear *similar* to a composition of the flows from intermediate constriction levels, and we show the way that this effect is rooted in the basic mechanics of the system, explaining why this causes the airflow to appear abnormal at certain points.

Extrapolating from this, we find a particular worst-case scenario wherein the quick correction from one volume to the “target” volume for the pleural pressure causes an extreme spike in the airflow velocity.

And finally, we show by asymmetric constriction that the primary source of resistance is not coming from the trachea. This is not *necessarily* incorrect, but it is certainly interesting, considering that prior studies have shown that the majority of airflow resistance in the lungs comes from the larger conducting airways. One possible explanation for this is the exact method we were using for whole lung constriction – in practice it *may* be more likely that typical airway constriction (e.g., from asthma) has a greater proportional effect on the larger airways.

5.2 Limitations and further work

There are of course a number of areas of possible improvement for the our experiments – a number of which have been briefly mentioned already, but they bear repeating. From a purely technical standpoint, it’s certainly possible to obtain more efficient models with a better matrix factorisation algorithm; GMRES will likely perform much better, but perhaps the most significant gains in simulation size and speed would come from parallel factorisation.

There are also a number of avenues for improvement in the accuracy of the simulation: An immediate improvement would be to use models synthesized from lung scans, as in [3]. But particularly as we increase constriction, it is also unreasonable to expect that the pleural pressure will remain the same – a model of pleural pressure that reacts to the lung volume in a similar way to humans may provide a more accurate result when looking at severe constriction.

Looking forward, there are possible applications of this research outside of this field – fast and efficient simulation provides a key opportunity to use this tool to provide data for data-intensive applications, like machine learning (in [15], for example, data was gathered from a physical system where it could have been done by modifying this software).

There are also possibilities within this space. Given the results on maximum flow acceleration, there may room for new multiple-breath washout indices that are more sensitive to constriction that is not as severe.

References

- [1] A. Ben-Tal. Simplified models for gas exchange in the human lungs, Jan 2006. URL <http://dx.doi.org/10.1016/j.jtbi.2005.06.005>.
- [2] Forum of International Respiratory Societies. The global impact of respiratory disease – third edition, 2021. URL http://www.firsnet.org/images/publications/FIRS_Master_09202021.pdf.
- [3] B. H. Foy, D. Kay, and R. Bordas. Modelling responses of the inert-gas washout and mri to bronchoconstriction, Jan 2017. URL <http://dx.doi.org/10.1016/j.resp.2016.09.009>.
- [4] B. Haefeli-Bleuer and E. R. Weibel. Morphometry of the human pulmonary acinus, Apr 1988. URL <http://dx.doi.org/10.1002/ar.1092200410>.
- [5] A. J. Hallett S, Toro F. Physiology, tidal volume, Jan 2022. URL <https://www.ncbi.nlm.nih.gov/books/NBK482502/>.
- [6] F. S. Henry, C. J. Llapur, A. Tsuda, and R. S. Tepper. Numerical modelling and analysis of peripheral airway asymmetry and ventilation in the human adult lung, Jun 2012. URL <http://dx.doi.org/10.1115/1.4006809>.
- [7] V. Hoffstein. Relationship between lung volume, maximal expiratory flow, forced expiratory volume in one second, and tracheal area in normal men and women, Nov 1986. URL <http://dx.doi.org/10.1164/arrd.1986.134.5.956>.
- [8] K. S. Kamel, G. Lau, and M. D. Stringer. In vivo and in vitro morphometry of the human trachea, Jul 2009. URL <http://dx.doi.org/10.1002/ca.20815>.
- [9] J. Neder, S. Andreoni, A. Castelo-Filho, and L. Nery. Reference values for lung function tests: I. static volumes, Jun 1999. URL <http://dx.doi.org/10.1590/S0100-879X1999000600006>.
- [10] M. Ochs, J. R. Nyengaard, A. Jung, L. Knudsen, M. Voigt, T. Wahlers, J. Richter, and H. J. G. Gundersen. The number of alveoli in the human lung, Jan 2004. URL <http://dx.doi.org/10.1164/rccm.200308-1107oc>.
- [11] M. Paiva. Gaseous diffusion in an alveolar duct simulated by a digital computer, Dec 1974. URL [http://dx.doi.org/10.1016/0010-4809\(74\)90030-5](http://dx.doi.org/10.1016/0010-4809(74)90030-5).
- [12] T. Pedley, R. Schroter, and M. Sudlow. Energy losses and pressure drop in models of human airways, Jun 1970. URL [http://dx.doi.org/10.1016/0034-5687\(70\)90093-9](http://dx.doi.org/10.1016/0034-5687(70)90093-9).
- [13] T. Pedley, R. Schroter, and M. Sudlow. The prediction of pressure drop and variation of resistance within the human bronchial airways, Jun 1970. URL [http://dx.doi.org/10.1016/0034-5687\(70\)90094-0](http://dx.doi.org/10.1016/0034-5687(70)90094-0).

- [14] A. W. Sheel, J. A. Guenette, R. Yuan, L. Holy, J. R. Mayo, A. M. McWilliams, S. Lam, and H. O. Coxson. Evidence for dysanapsis using computed tomographic imaging of the airways in older ex-smokers, Nov 2009. URL <http://dx.doi.org/10.1152/japplphysiol.00562.2009>.
- [15] D. Suo, N. Agarwal, W. Xia, X. Chen, U. Ghai, A. Yu, P. Gradu, K. Singh, C. Zhang, E. Minasyan, J. LaChance, T. Zajdel, M. Schottdorf, D. Cohen, and E. Hazan. Machine learning for mechanical ventilation control. 2021. doi: 10.48550/ARXIV.2102.06779. URL <https://arxiv.org/abs/2102.06779>.
- [16] M. H. Tawhai and P. J. Hunter. Multibreath washout analysis: modelling the influence of conducting airway asymmetry, Sep 2001. URL [http://dx.doi.org/10.1016/S0034-5687\(01\)00239-0](http://dx.doi.org/10.1016/S0034-5687(01)00239-0).
- [17] W. M. Thurlbeck. Postnatal human lung growth., Aug 1982. URL <http://dx.doi.org/10.1136/thx.37.8.564>.
- [18] S. Verbanck and M. Paiva. Model simulations of gas mixing and ventilation distribution in the human lung, Dec 1990. URL <http://dx.doi.org/10.1152/jappl.1990.69.6.2269>.
- [19] E. R. Weibel. *Morphometry of the human lung*. Springer, Berlin, Germany, 1963 edition, dec 2013.
- [20] E. R. Weibel, B. Sapoval, and M. Filoche. Design of peripheral airways for efficient gas exchange, Aug 2005. URL <http://dx.doi.org/10.1016/j.resp.2005.03.005>.

Appendix A: Extended equations

In subsection 3.2, the function controlling pleural pressure is referenced. It is defined here, using a minimum $P_{\text{pl}_{\min}}$, maximum $P_{\text{pl}_{\max}}$ and initial pressure $P_{\text{pl}_{\text{init}}}$. The period is T .

$$P_{\text{pl}}(t_n) = M - A \cos \left(\frac{2\pi}{T} t_n + \cos^{-1} \left(\frac{M - P_{\text{pl}_{\text{init}}}}{A} \right) \right) \quad (12)$$

where

$$A = \frac{P_{\text{pl}_{\max}} - P_{\text{pl}_{\min}}}{2} \quad (\text{amplitude})$$

$$M = \frac{P_{\text{pl}_{\max}} + P_{\text{pl}_{\min}}}{2} \quad (\text{mean})$$

This function has the property that – if the initial value is not the minimum or maximum value – it is always increasing at $t_n = 0$. If the initial value is the minimum, $P_{\text{pl}}(t_n)$ is not technically increasing at $t_n = 0$, but it will be at $t_n = \epsilon$.